Materials Advances

ROYAL SOCIETY OF CHEMISTRY

PAPER

View Article Online
View Journal | View Issue

Cite this: *Mater. Adv.*, 2025, 6, 2435

Optimized porous alkali-activated material for superior dye removal: synthesis and performance analysis

Youssef Ettahiri, *[ab] Abdessalam Bouddouch,[c] Brahim Akhsassi,[b] Anass Khali,[b] Lahcen Bouna,[b] Abdeljalil Benlhachemi[b] and Luis Pérez-Villarejo *[ad]

Received 22nd October 2024,
Accepted 16th March 2025

DOI: 10.1039/d4ma01065e

rsc.li/materials-advances

In this study, a porous alkali-activated material was employed as an efficient adsorbent for the removal of methylene blue (MB). The material, referred to as GP-NC, was synthesized through geopolymerization by activating natural clay (NC) with an alkaline activator solution and incorporating H_2O_2 to induce pore formation within the matrix. The structure, microstructure, and morphology of the samples were extensively characterized using a variety of techniques, including XRD, ^{29}Si and ^{27}Al MAS NMR, FTIR, DTA/TGA, BET, SEM, and TEM. The formation of alkali-activated material was confirmed through XRD, ^{29}Si, and ^{27}Al MAS NMR analyses. The GP-NC exhibited a significantly higher surface area (30.23 $m^2\ g^{-1}$) compared to NC (15.28 $m^2\ g^{-1}$). Additionally, FTIR and SEM analyses validated the successful adsorption of methylene blue (MB) onto the alkali-activated material. These findings offer valuable insights into the structural properties and adsorption performance of GP-NC, emphasizing its potential as an effective adsorbent for methylene blue removal from aqueous solutions. The sorption process was best described by the pseudo second order kinetic model and the Langmuir isotherm model, with a maximum adsorption capacity of 98.95 mg g^{-1} at 25 °C. Furthermore, the calculated mean free energy (E) using the Dubinin-Radushkevich model suggests that the adsorption of MB onto GP-NC follows a physisorption mechanism.

1. Introduction

In recent years, the increasing discharge of dyes into the environment has become a pressing environmental concern.[1] These dyes, commonly used in industries such as textile, paper, and printing, pose a significant threat to both ecosystems and human health due to their persistence, toxicity, and potential carcinogenicity.[2–6] Various wastewater treatment techniques have been adopted, including aerobic and anaerobic treatment, coagulation-flocculation, ion exchange, membrane filtration, electrochemical methods, advanced oxidation processes, and adsorption.[7–14] Adsorption is an effective and cost-efficient method for pollutant removal, offering simplicity, affordability, and high efficiency in wastewater treatment. It requires minimal operational complexity, making it accessible for various applications while effectively removing contaminants such as heavy metals, dyes, and organic compounds.[15,16] One promising strategy for enhancing adsorption-based treatment is the use of alkali-activated materials.[17–19] These amorphous inorganic materials are formed through the reaction of aluminosilicate precursors with alkaline activators, offering excellent adsorption capacity and environmental sustainability.[20,21] These materials possess several desirable characteristics, including excellent mechanical strength, thermal stability, and chemical resistance, making them ideal candidates for diverse applications.[22–24] The creation of porosity into the alkali-activated structure offers several advantages for dye removal, including increased surface area and pore volume, enhanced mass transfer, and improved accessibility to the active sites.[13,25,26] Moreover, the introduction of functional groups onto the surface of the alkali-activated materials can enhance its affinity for dyes through electrostatic interactions or chemical bonding.[26] The porous structure of alkali-activated materials provides many active sites for dye adsorption, while the interconnected pore network facilitates the diffusion of dye molecules into the bulk material. Furthermore, the use of

[a] *Center for Advanced Studies in Earth Sciences, Energy and Environment (CEACTEMA), University of Jaén, Campus Las Lagunillas, s/n, 23071, Jaén, Spain. E-mail: lperezvi@ujaen.es*
[b] *Materials and Environment Laboratory (LME), Faculty of Sciences, Ibn Zohr University, Dakhla city B.P. 8106, Agadir, Morocco. E-mail: youssef.ettahiri@edu.uiz.ac.ma*
[c] *Laboratory of Physical Chemistry of Materials (LPCM), Department of Chemistry, Faculty of Science, Chouaïb Doukkali University, El Jadida, Morocco*
[d] *Department of Chemical, Environmental, and Materials Engineering, Higher Polytechnic School of Linares, University of Jaen, Campus Científico-Tecnológico, Cinturón Sur s/n, 23700, Linares, Spain*

porous alkali-activated materials offers several advantages, including their abundance, low-cost precursors, and environment-friendly nature.[27,28] To enhance the adsorption capacity and efficiency of alkali-activated materials for dye removal, the incorporation of H_2O_2 has gained significant attention.[29] The combination of H_2O_2 with alkali-activated matrices offers unique properties that can be exploited for efficient dye removal from aqueous solutions. Hydrogen peroxide (H_2O_2) plays a crucial role in creating porosity in alkali-activated materials, which can enhance their adsorption capacity, making them effective for applications like removing methylene blue from solutions.[29] When added to the alkali-activated material mix, H_2O_2 decomposes in the alkaline environment, releasing oxygen gas that forms bubbles within the paste. These bubbles create a network of interconnected pores, increasing the material's surface area and porosity.

In this study, hydrogen peroxide (H_2O_2) was introduced to generate porosity in alkali-activated kaolinite-rich natural clay, a widely available and sustainable precursor, for the removal of methylene blue dye from aqueous solutions. The structural properties of the synthesized adsorbent were systematically characterized to elucidate its composition, porosity, and surface morphology. Additionally, a series of experimental investigations were conducted to analyze the adsorption mechanism at the solid–liquid interface, with a particular focus on *in situ* electrostatic interactions, providing valuable insights into the underlying adsorption processes.

2. Materials and methods

2.1. Sampling and alkali-activated material preparation

The natural clay (NC) utilized in this study is sourced from Assa-Zag province situated in north of the Moroccan Sahara (Fig. 1). The initial step involved in the process is the grinding and sieving of the natural clay sample to obtain particles with a size of 70 μm. This sample is referred to as NC. However, *meta*-NC is naturel clay calcined at 600 °C for 4 h. The alkali-activated material was named GP-NC, this is created by adding 6 g of *meta*-NC to a previously prepared alkaline activation solution. The activation solution is formed by sodium silicate solution prepared by dissolving the desired amount of SiO_2 (1.5 g) and NaOH (1.5 g) in 15 mL of distilled water by stirring for 10 minutes, which is vigorously stirred until it forms a uniform gel, subsequently adding H_2O_2 (0.25 g) to the mixture of metakaolin and alkali activator. The resulting mixture, GP-NC, is then stirred for 30 minutes to ensure homogeneity and subsequently placed in an oven at 70 °C for 3 days (Fig. 2). The solid product is then crushed to facilitate structural characterization and made the adsorption tests.

2.2. Characterizations methods

The X-ray diffraction (XRD) data for the natural clay and the alkali-activated material prepared were obtained by measuring diffraction patterns using a Bruker D8 Advance Twin diffractometer. The measurements were conducted with $K_{\alpha Cu}$ irradiation at a wavelength of λ = 1.5418 Å, covering a range of 5–60° 2θ, with a time of reckoning of 0.3 s and a step scanning interval of 0.05°. Direct-polarized ^{27}Al and ^{29}Si NMR measurements were performed on a Unity Inova 300 spectrometer (^{1}H resonance frequency of 300 MHz, field strength of 7.05 T). Each sample was packed in a 4-mm ZrO_2 rotor and magic angle spinning at 10 kHz was employed to reduce quadrupolar line broadening effects. The aluminum spectra were referenced with respect to a 1 mol L^{-1} solution of $Al(NO_3)_3$ (chemical shift = 0.00 ppm) and the silicon spectra were referenced to Q_8M_8 (chemical shift = 11.45 ppm relative to TMS). For aluminum spectra, 4000 scans were collected (acquisition time 5.12 ms, recycle time 1 s, 90-degree pulse width of 0.8 μs) with 512 points in the FID and for silicon spectra, 2800 scans were

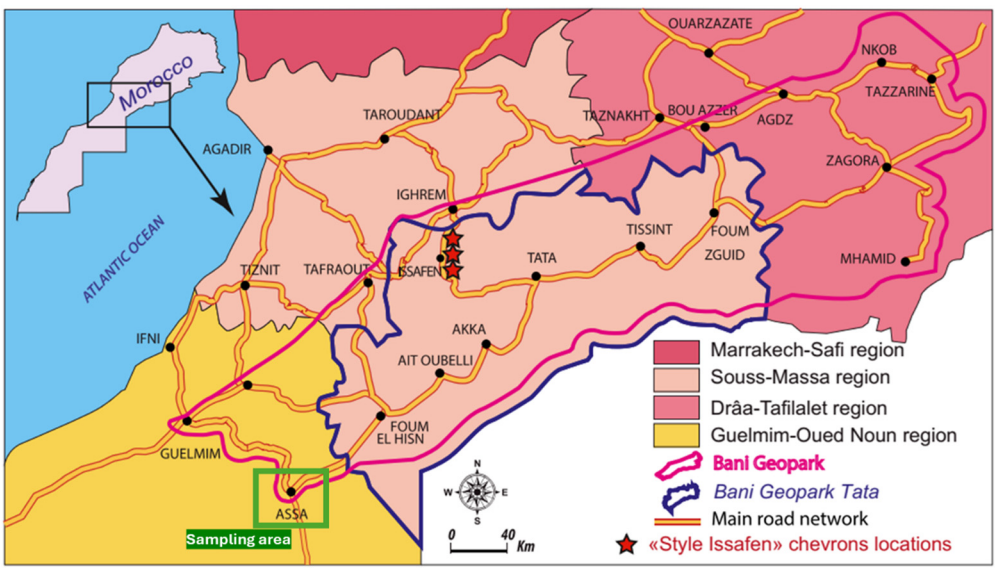

Fig. 1 Map showing the location of Assa.[30]

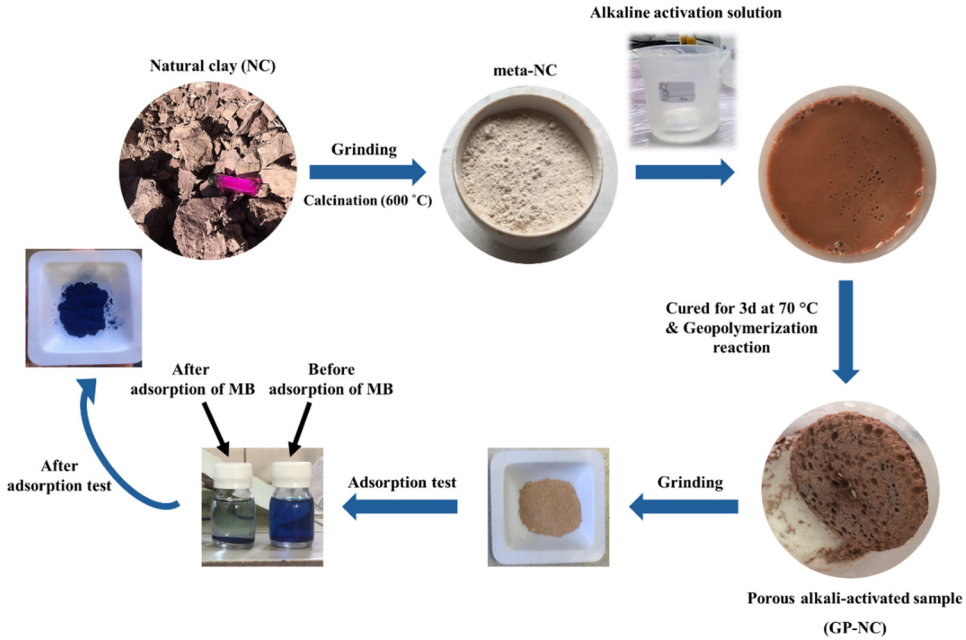

Fig. 2 Schematic preparation of the porous alkali-activated material.

collected (acquisition time 5.12 ms, recycle delay 30 s, 45-degree pulse width of 1.5 μs) with 128 points. Spectra were normalized by the maximum value of the spectrum for plotting. FTIR spectra were obtained using an IRAffnity-1S Shimadzu spectrophotometer, spanning the range of 400–4000 cm^{-1}. For TGA and DTA analyses, a Q500 TA instrument was employed. The NC and GP-NC samples were subjected to temperature ranges of 25–1000 °C at a rate of 10 °C min^{-1}. The specific surface area of the NC and GP-NC samples was determined using the BET method, and the N_2 adsorption/desorption isotherms at 77 K were measured using a 3FLEX (Micromeritics, USA) analyzer. Prior to measurement, each sample was outgassed at 200 °C for 12 hours. To examine the morphology of each alkali-activated preparation, SEM analysis was conducted using a JEOL TSM-IT100 operating at a voltage of 20 KeV. TEM analysis was performed using a Tecnai G2 F20 microscope operating at 200 kV. The zero charge point (PZC) of the GP-NC was determined *via* potentiometric titration method reported by Fiol and Villaescusa.[31]

2.3. Results and discussion

2.3.1. Samples characterization. Fig. 3a presents XRD diffractograms of natural clay (NC), natural clay calcined at 600 °C (*meta*-NC) and prepared alkali-activated GP-NC. The XRD patterns of the natural clay show the presence of kaolinite (JCPDS: 80-0885), muscovite (JCPDS: 07-0025), and quartz (JCPDS: 46-1045). After the curing at 600 °C, we observe the disappearance of kaolinite peaks, and the muscovite has transformed into potassium aluminum silicate phase (JCPDS: 046–0741),. In the synthesized GP-NC, an amorphous hump is visible in the 15–36° 2θ angular range, indicating successful alkali activation and transformation of the kaolinite into an amorphous alkali-activated material.[6]

The ^{27}Al and ^{29}Si spectra of the natural clay (NC), calcined clay (*meta*-NC), and alkali-activated prepared (GP-NC) are shown in Fig. 3b and c. In the ^{27}Al spectrum (Fig. 3b), the appearance of very intense six-coordinated aluminum species at 0.64 ppm in the raw clay suggests and highlights the presence of kaolinite in natural clay.[32] Upon calcination (*meta*-NC), the transformation of six-coordination Al(VI) to four-coordination Al(IV) is observed, indicating the metaphase has been achieved. This transformation is a common occurrence during the calcination process and is consistent with the removal of water and other volatile components.[33] However, a slight shoulder around 30 ppm is attributable to Al(V), which is the reactive component of metakaolin and develops during calcination of raw kaolin clay.[34,35] For GP-NC sample, the narrow and very intense peak obtained at approximately 60 ppm suggests the formation of Al(IV) species characterizing the alkali-activated materials matrix.

Turning to the ^{29}Si spectrum (Fig. 4c), the presence of a small peak at −107 ppm corresponds to quartz impurities within the clay. Calcination leads to an increase in intensity at more negative chemical shifts, reflecting the dehydroxylation of the kaolinite.[35–37] This chemical shift indicates the removal of hydroxyl groups as a necessary step for geopolymerization. Interestingly, in the alkali-activated spectrum, a shift towards more negative chemical shifts compared to *meta*-NC suggests the influence of the activation solution, typically containing sodium silicate.[38] This shift indicates the interaction between the *meta*-NC and the activating solution, leading to changes in the chemical environment of Si. This alteration in chemical shift signifies the dissolution of silicate species from the clay matrix and their incorporation into the alkali-activated network during the geopolymerization process.[39]

Fig. 3d illustrates the FTIR spectra of the natural clay (NC), the natural clay calcined at 600 °C (*meta*-NC), and the alkali-activated

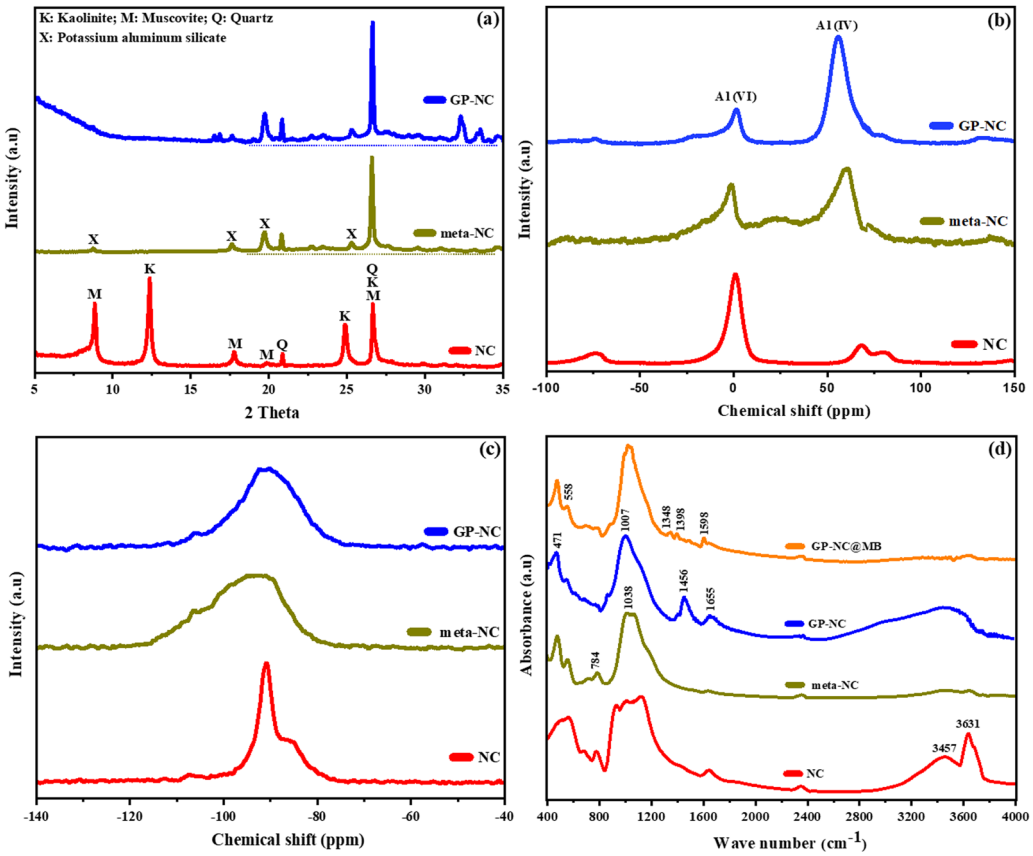

Fig. 3 (a) XRD data, (b) ^{27}Al (a) ^{29}Si (c) NMR and (b) FTIR spectra.

prepared (GP-NC). The band observed at 784 cm^{-1} is associated with quartz Si–O bond vibrations.[26] Bands between 1000 cm^{-1} and 1100 cm^{-1} correspond to asymmetric stretching vibrations of Si–O–T (T = Si or Al). The shifting position from 1038 cm^{-1} (in the *meta*-NC) to 1007 cm^{-1} in alkali-activated GP-NC indicates successful activation of the NC phase with the alkaline activation solution and the formation of an alkali-activated matrix. The absence of the Si-O-T symmetric stretching vibrations, usually seen at 797 cm^{-1} and 802 cm^{-1} in *meta*-NC, within the alkali-activated material spectrum, further illustrates this behavior, this absence indicates the breakdown of the original octahedral structure of the kaolinite raw.[15,40] In the case of alkali-activated prepared GP-NC, new vibrational bands appear, the band centered at about 1456 cm^{-1} is attributed to carbonate. The large band appearing in the interval 2800–3800 cm^{-1} is attributable to the OH vibration of water adsorbed in pores of alkali-activated prepared.[6,41] The sample GP-NC@MB (Fig. 3d), obtained after methylene blue adsorption, exhibits new vibrational bands at 1348, 1398, and 1598 cm^{-1}, attributed to the bending vibrations of methylene blue molecules adsorbed onto the GP-NC surface.[6] Additionally, the narrowing of the OH vibration band (3500–3664 cm^{-1}) suggests modifications in hydrogen bonding interactions, further confirming the successful adsorption of MB molecules.[42]

Fig. 4 illustrates the nitrogen adsorption–desorption isotherms and mesopore size distribution, obtained using the BJH method, for natural clay (NC), and alkali-activated prepared (GP-NC). Both samples exhibit hysteresis loops type IV, indicating the presence of mesoporous characteristics based on the IUPAC classification for mesoporous materials (Fig. 4a). The specific surface area (S_{BET}) values for the NC, and the GP-NC are provided in Table 1. The NC sample demonstrates a mesoporous nature, which is further confirmed by the BJH curves in Fig. 4b, showing specific surface area of 15.28 m^2 g^{-1}. In contrast, the GP-NC sample, prepared with H_2O_2, exhibits the presence of mesopores, with specific surface area of 30.23 m^2 g^{-1}. Notably, the porous alkali-activated prepared with H_2O_2 shows a significant enhancement in porosity, approximately twice as high than that of Kao. Furthermore, all samples demonstrate a maximum pore width ranging from 3 to 5 nm.

Fig. 5 presents the thermograms (TGA) and differential thermal analysis (DTA) results for natural clay (NC), *meta*-NC, and GP-NC as a function of heating temperature. The TGA thermogram for NC shows an initial weight loss of 1.1% below 200 °C, primarily due to the removal of surface water from the kaolinite sheets, followed by the loss of fixed water.[26] A prominent endothermic peak at 500 °C corresponds to the dehydroxylation of kaolinite, leading to a 7.2% weight loss.[6,43] In contrast, GP-NC shows a significant increase in mass loss (11.2%) compared to both the natural clay and calcined fraction. This increased loss is mainly attributed to the release of

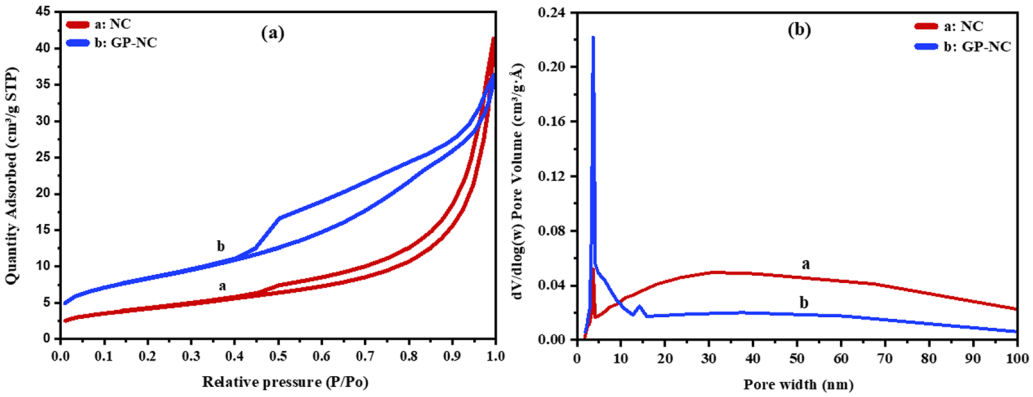

Fig. 4 (a) Nitrogen adsorption–desorption isotherms, (b) Mesopore size distribution curves determined by BJH method of NC, and GP-NC.

Table 1 Specific surface area S_{BET} of NC and GP-NC

Sample	S_{BET} (m^2 g^{-1})
NC	15.28
GP-NC	30.23

physisorbed water from the porous structure and surface of the prepared geopolymers, highlighting the development of key characteristics such as porosity, which arise from the alkali-activated synthesis conditions.[44]

Fig. 6 presents a comparative analysis of the structural characteristics of natural clay calcined (*meta*-NC), alkali-activated material (GP-NC) and alkali-activated after adsorption of methylene blue (GP-NC@MB) based on SEM imaging. Fig. 6a–c exhibit the characteristic platelet morphology of metakaolin,[26,40] as confirmed by XRD analysis. In contrast, Fig. 6d–f reveal a significant morphological transformation in GP-NC, with a well-developed network of systematically arranged pores. This structural modification is primarily attributed to the effect of H_2O_2 during the alkaline activation process, which enhances porosity. The densification observed in the microstructure of GP-NC compared to *meta*-NC is due to the polymerization and polycondensation of aluminosilicate phases, forming an integrated GP-NC network. Additionally, the micrographs display capillary pores distributed throughout the GP-NC matrix, indicating that the blowing agent influences both the macro- and microstructure of the GP-NC. Notably, the presence of cracks and capillary pores on the surface of GP-NC provides accessible pathways for adsorbates, facilitating their diffusion toward active sites within the framework during the adsorption process.[29,45] The GP-NC@MB sample, obtained after methylene blue adsorption (Fig. 6g–i), exhibits a more homogeneous surface with decreased porosity compared to the initial material (GP-NC). Additionally, EDS analysis of the GP-NC@MB sample, as presented in Table 2, detects the presence of carbon (C) and sulfur (S), confirming the effective adsorption and stable fixation of methylene blue molecules on the surface and within the pores of the GP-NC sample. Examining the TEM images in Fig. 7a and b for *meta*-NC, a clear illustration of the lattice morphology characterizing the metakaolin is observed.[46] TEM analysis of the GP-NC reveals the presence of nanoparticles within two distinct gel-phase morphologies at the nanometer scale (Fig. 7c and d). The first corresponds to the amorphous gel phase, characteristic of the alkali-activated material (GP-NC) matrix, while the second consists of crystalline nanoparticles, likely remnants of unreacted precursor minerals such as quartz and muscovite that did not fully participate in the geopolymerization reaction.[47] These findings

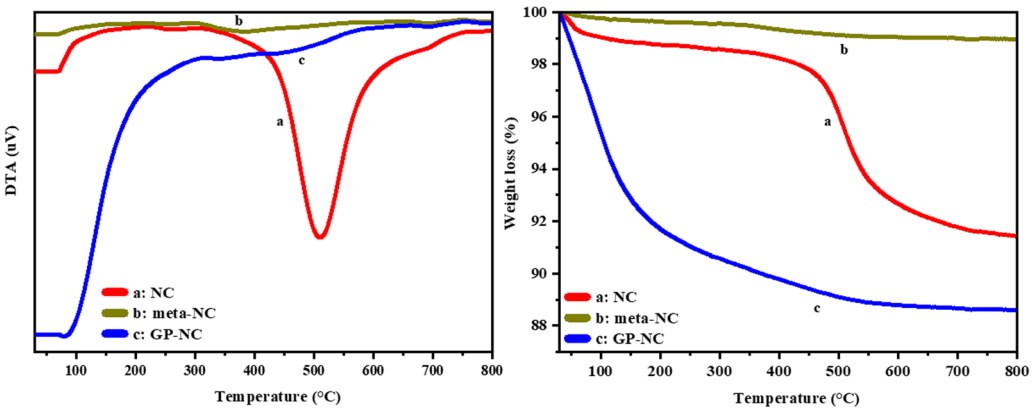

Fig. 5 TGA/DA curves of NC, *meta*-NC, and GP-NC.

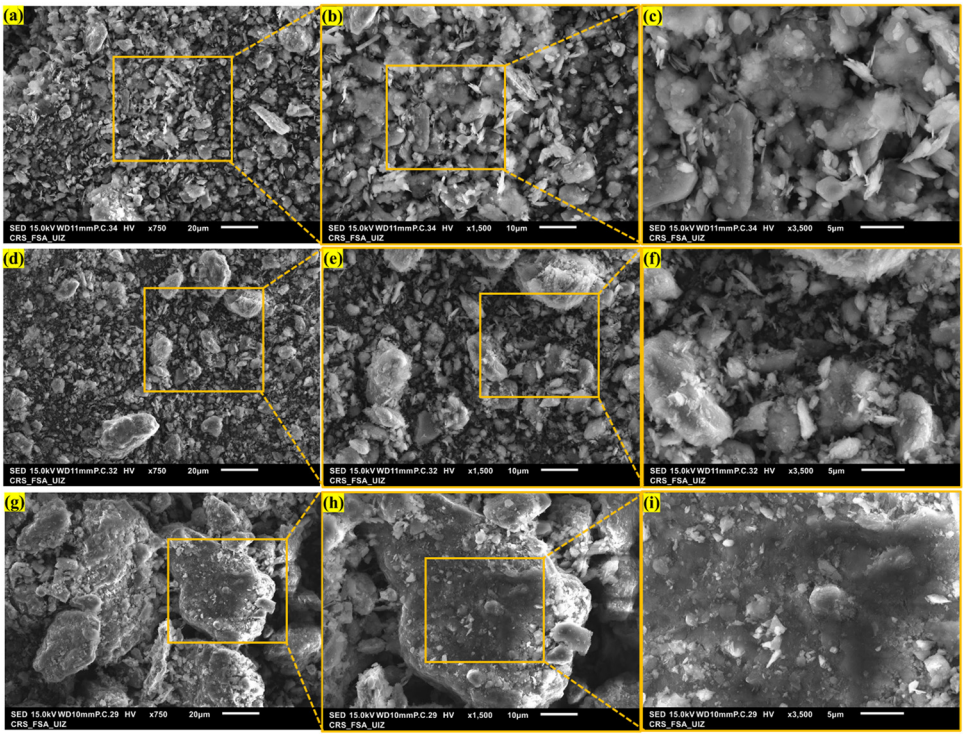

Fig. 6 SEM and TEM micrographs of *meta*-NC (a–c), GP-NC (d–f), and GP-NC@BM (g–i).

Table 2 EDS atomic percentage of, *meta*-NC, GP-NC, and GP-NC@MB

Sample	O	Si	Al	K	Na	C	Ti	Fe	N	S
meta-NC	57.40	13.08	11.30	1.39	0.68	14.96	0.24	0.94	—	
GP-NC	55.08	12.01	7.15	0.76	3.03	21.32	0.16	—	—	
GP-NC@BM	57.92	17.66	8.44	0.92	3.25	9.64	—	—	1.48	0.69

are consistent with XRD results, further confirming the coexistence of both amorphous and crystalline phases in the alkali-activated material structure.

3. Adsorption studies

3.1. Effect of the adsorbent dose, contact time and pH on the MB dye adsorption

The effect of adsorbent concentration on MB removal is presented in Fig. 8a. This experiment was conducted under the following conditions: stirring time of 120 min, [MB] = 100 mg L^{-1}, temperature = 25 °C, and pH = 6. The removal percentage (%R) and the amount of adsorbed dye (q_e) at the remaining concentration were calculated using the following equations (eqn (1) and (2)), respectively.

$$q_{ads} = \frac{(C_0 - C_e) \times V}{M} \quad (1)$$

$$\%R = \frac{(C_0 - C_e) \times 100}{C_e} \quad (2)$$

while C_0 (mg L^{-1}) and C_e (mg L^{-1}) are the initial and equilibrium concentrations of MB solution, respectively; M (g) is the mass of adsorbent; and V (L) is the volume of adsorbate solution.

Fig. 8a illustrates the equilibrium adsorption capacity as a function of adsorbent dose. The results indicate that the percentage of MB removal increases with increasing adsorbent concentration. This can be attributed to the larger specific surface area and the greater number of available adsorption sites, which enhance dye uptake. However, beyond a concentration of approximately 3 g L^{-1}, saturation is reached. As shown in Fig. 8a, the MB removal efficiency reaches 99.45%, while the maximum adsorption capacity is approximately 35.47 mg g^{-1} at this optimal GP-NC dose. Based on these findings, an adsorbent concentration of 3 g L^{-1} will be used in subsequent studies.

The effect of contact time on the removal rate of methylene blue (MB) was investigated over a range of 5 to 180 minutes, and the variation in adsorption capacity is presented in Fig. 8b in this experiment, an initial MB concentration of 100 mg L^{-1}, a sorbent dose of 3 g L^{-1}, a temperature of 25 °C and pH of 6 were employed to evaluate the influence of contact time under ambient conditions. Fig. 8b illustrates the variation in MB adsorption as a function of contact time. The experimental data reveal that the amount of MB adsorbed increases with increasing contact time, reaching equilibrium at approximately 60 minutes, which signifies the saturation of available adsorption sites on the sorbent surface. More specifically, the maximum adsorption capacity was recorded at 60 minutes, with a value of 32 mg g^{-1}. The initial rapid increase in the removal rate can be attributed to fast external mass transfer, followed by a slower adsorption phase as equilibrium is approached.

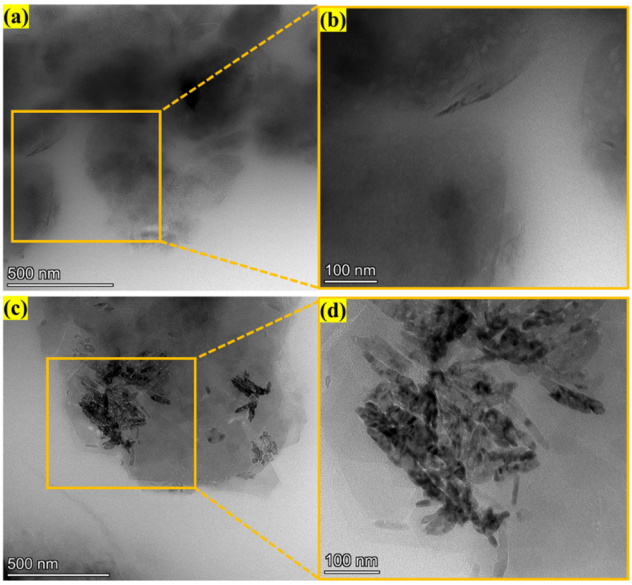

Fig. 7 TEM micrographs of *meta*-NC (a and b), GP-NC (c and d).

This latter phase is likely governed by internal mass transfer mechanisms, corresponding to the diffusion of MB molecules into the porous structure of the adsorbent.

The pH of the solution plays a critical role in the adsorption process, as it influences the surface charge of the adsorbent, the speciation of the dye molecules, and the overall adsorption mechanism. pH adjustments were made using 0.1 M hydrochloric acid (HCl) for acidification and 0.1 M sodium hydroxide (NaOH) for alkalization. The effect of pH on MB adsorption was studied over a range of 2 to 10 under controlled conditions: [MB] = 100 mg L^{-1}, m = 3 g L^{-1}, T = 25 °C, and t = 60 min. The results, presented in Fig. 8c, show that MB adsorption increases in alkaline conditions, reaching a maximum at pH 10 (pH_{pzc}= 5.7, Fig. 8d). This enhanced adsorption is primarily attributed to electrostatic interactions between the cationic MB dye and the negatively charged surface of the alkali-activated GP-NC adsorbent.[48] This result can be explained by the creation of new adsorption sites due to an increase in the negative charge density on the GP-NC surface. This increase is induced by the deprotonation of M–OH species under the influence of OH^- entities present in a basic medium, according to the following reaction.

$$M\text{–}OH + OH^- \rightarrow M\text{–}O^- + H_2O \text{ (M = Si ou Al)}$$

Similar observations have been reported in previous studies, indicating that at higher pH values, deprotonation of the adsorbent surface enhances cationic dye adsorption due to increased electrostatic attraction. Conversely, at lower pH values, MB removal efficiency decreases due to the protonation of adsorption sites, leading to electrostatic repulsion between the positively charged surface of GP-NC and the cationic MB molecules. Based on these findings, an equilibrium pH of 6 will be maintained for all subsequent experiments.

3.2. Adsorption kinetics

In order to study the mechanism of the adsorption process, The adsorption kinetics experiments of GP-NC were carried under

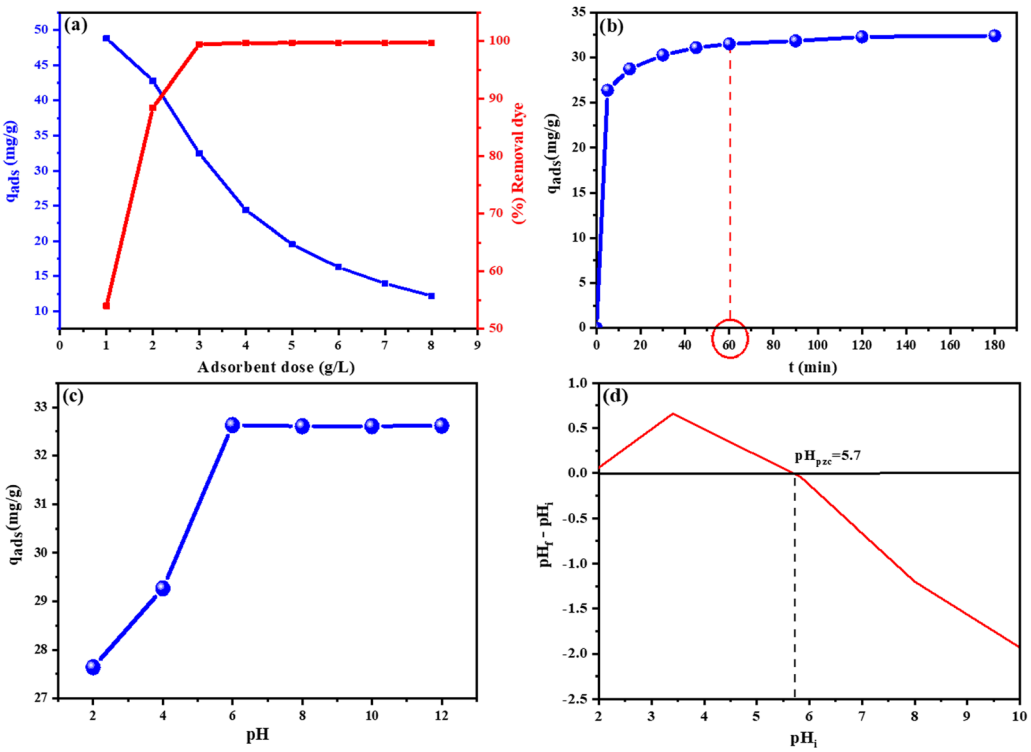

Fig. 8 (a) Effect of adsorbent dose; (c) effect of contact time; effect of pH on the adsorption of MB on GP-NC; (d) point zero charge (pH_{PZC}).

controlled conditions: time = 5–180 min, [MB] = 100 mg L^{-1}, m (GP-NC) = 3 g L^{-1}, T = 25 °C, t = 60 min and pH = 6. To analyze the kinetic data, different kinetic models like the pseudo first order, and pseudo second order, Intra-particle diffusion were followed. The three models followed using these equations (eqn (3), (4) and (5)), respectively:

$$q_t = q_e\,(1 - \exp^{-K_1 t}) \quad (3)$$

$$q_t = \frac{K_2 q_e^2 t}{1 + K_2 q_e t} \quad (4)$$

$$q_t = K_{int}\sqrt{t} + C \quad (5)$$

while q_e and q_t are the adsorbed amounts at equilibrium and at times t, respectively. The equilibrium rate constants K_1 (min^{-1}), K_2 (g mg^{-1} min^{-1}), and K_{int} (mg g^{-1} $min^{-0.5}$) pertain to the adsorption kinetics of pseudo first order, pseudo second order, and intra-particle diffusion, respectively. The constant C (mg g^{-1}) provides insights into the boundary layer thickness.

As shown in Fig. 9a, the adsorption capacity of GP-NC increased rapidly within the first 60 minutes, followed by a slower rise until it reached a relatively stable value. After 60 minutes, no significant changes in adsorption capacity were observed, indicating that equilibrium was achieved at this point. To analyze the adsorption kinetics, the data were fitted to pseudo first order, pseudo second order, and intra-particle diffusion models using nonlinear equations. The fitting curves for these models are presented in Fig. 9a, with the corresponding parameters summarized in Table 3. Among the models, the pseudo second order model provided the best fit for MB adsorption onto GP-NC, as indicated by its higher correlation coefficient (R^2 = 0.997) compared to the pseudo first order model (R^2 = 0.988) and intra-particle diffusion (R^2 = 0.504).

3.3. Adsorption isotherms

To further understand the mechanism of adsorption of MB dye onto GP-NC, three classical adsorption models, *i.e.*, the Langmuir, Freundlich, and Dubinin-Radushkevish isotherm models were applied. The three models were followed using these equations

Table 3 Kinetic parameters of GP-NC for MB removal

Models	Parameters	
Pseudo first order	R^2	0.988
	K_1 (min^{-1})	0.366
	q_e (mg g^{-1})	31.19
Pseudo second order	R^2	0.997
	K_2 (g mg^{-1} min^{-1})	0.026
	q_e (mg g^{-1})	32.09
Intra-particle diffusion	R^2	0.504
	K_{int} (mg g^{-1} $min^{-0.5}$)	1.721
	C (mg g^{-1})	15.71

(eqn (6), (7) and (8)), respectively:[49,50]

$$q_e = \frac{q_m K_L C_e}{1 + K_L C_e} \quad (6)$$

$$q_e = K_f C_e^{1/n} \quad (7)$$

$$q_e = q_m \exp\left(-K_{DR}\left(RT \ln\left(1 + \frac{1}{C_e}\right)\right)^2\right) \quad (8)$$

The mean free energy of adsorption, E (kJ mol^{-1}) is derived from the following equation (eqn (9)):

$$E = \frac{1}{\sqrt{2K_{DR}}} \quad (9)$$

To differentiate between physical and chemical sorption, the mean free energy (E) per molecule of the adsorbate serves as a crucial indicator. If E < 8 kJ mol^{-1}, the process is categorized as physisorption, whereas E > 16 kJ mol^{-1} signifies chemisorption. When 8 kJ mol^{-1} < E < 16 kJ mol^{-1}, the adsorption mechanism is primarily governed by ion exchange.[51,52]

Where C_e is the equilibrium concentration of dye (mg L^{-1}), q_e (mg g^{-1}) is the quantity adsorbed at equilibrium, q_m (mg g^{-1}) is the maximum adsorption capacity for complete monolayer coverage, K_L is Langmuir isotherm constant (L mg^{-1}), K_F is Freundlich isotherm constant (mg g^{-1}), n refers to adsorption intensity. K_{DR} (mol^2 kJ^{-2}) is Dubinin-Radushkevich constant,

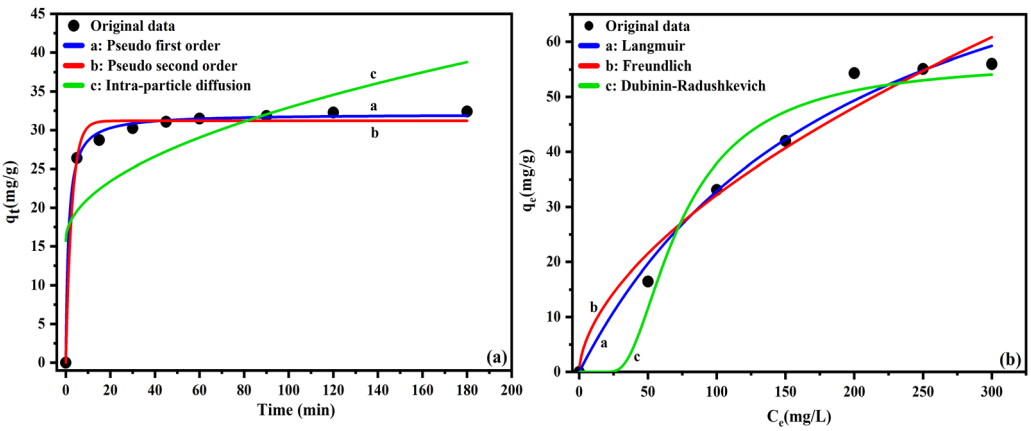

Fig. 9 (a) adsorption kinetics, (b) adsorption isotherms.

Table 4 Isotherms parameters for the adsorption of MB onto GP-NC

Isotherm models	Parameters	
Langmuir	R^2	0.994
	K_L (L mg^{-1})	0.005
	q_m (mg g^{-1})	98.95
Freundlich	R^2	0.927
	K_f (mg g^{-1}) (L mg^{-1})$^{1/n}$	2.23
	n	1.73
Dubinin-Radushkevish	R^2	0.967
	K_{DR} (mol^2 KJ^{-2})	4037.65
	q_m (mg g^{-1})	56.55
	E (KJ mol^{-1})	0.011

T is the absolute temperature (K), and R is the universal gas constant, 8.314 J mol^{-1} K^{-1}.

The adsorption equilibrium experiments of GP-NC were conducted by stirring 3 g L^{-1} of GP-NC in MB solutions with varying initial concentrations (50–300 mg L^{-1}) at 25 °C and pH 6 for 60 minutes. As depicted in Fig. 9b, the adsorption capacity of GP-NC exhibits a rapid increase with the rise in the initial MB concentration within the range of 50–200 mg L^{-1}, after which it plateaus, indicating saturation of available active sites. The adsorption capacity optimization from 17 to 55 mg g^{-1} is attributed to the balance between the number of available adsorption sites and the initial MB molecules in solution. The adsorption isotherm models fitted to the experimental data indicate that the Langmuir model provides the best fit, as indicated by its higher R^2 value compared to the Freundlich and Dubinin-Radushkevich models (Table 4). This suggests that the adsorption of MB dye onto GP-NC occurs primarily through monolayer adsorption on a homogeneous surface, confirming the strong affinity between MB molecules and GP-NC active sites. The saturation behavior at higher concentrations implies that once the monolayer coverage is complete, no further significant adsorption can occur, reinforcing the Langmuir model's applicability to this system. Additionally, the calculated mean free energy (E) of 0.011 kJ mol^{-1} confirms that the adsorption of MB onto GP-NC follows a physisorption mechanism. This suggests that the process is predominantly driven by electrostatic interactions and van der Waals forces.

3.4. Adsorption performances and mechanism

The comparison of GP-NC's maximum adsorption capacity, along with its advantages and disadvantages relative to other adsorbents for MB dye removal, demonstrates its superiority. GP-NC shows significantly higher adsorption of MB dye compared to many other adsorbents. This superior performance is mainly due to key characteristics, such as surface charge and pore structure. These properties are further evidenced in the interaction mechanisms involved in MB adsorption. The adsorption of MB onto GP-NC involves multiple mechanisms, including electrostatic attraction, hydrogen bonding, and π–π interactions.[26] The negatively charged surface of GP-NC, primarily from the aluminum (Al) atoms, attracts the positively charged MB molecules *via* electrostatic forces. Additionally, hydrogen bonding can occur between the hydroxyl groups on the GP-NC surface and the amine groups in MB. π–π interactions between the aromatic rings of MB and the silicate/aluminosilicate framework of the material further stabilize the adsorption process. Together, these mechanisms contribute to the efficient removal of MB dye, making GP-NC an effective adsorbent for wastewater treatment. These results highlight GP-NC's exceptional ability to remove cationic dyes, demonstrating the highest adsorption capacity among the materials tested (Table 5).

3.5. Limitations, challenges, and future research recommendations

The modified GP-NC adsorbent demonstrates significant potential for removing organic pollutants, such as methylene blue, from contaminated water. Natural clays, as precursors of alumino-silicate materials for GP-NC preparation, offer several advantages. They are abundant, widely available, and cost-effective compared to industrial waste materials like fly ash or slag. The chemical composition of natural clays, particularly their alumino-silicate minerals, makes them highly reactive when treated, promoting effective geopolymerization. However, practical application in wastewater treatment systems presents some challenges. The presence of complex pollutant mixtures and competing ions in real-world conditions may reduce adsorption efficiency, highlighting the need for further studies under more realistic scenarios. While GP-NC shows high adsorption capacity, issues such as regeneration and reusability could limit long-term performance and cost-effectiveness. Structural degradation over multiple adsorption–desorption cycles and potential leaching of modification agents poses concerns for environmental safety. To address these limitations, future research should focus on enhancing material stability through surface modifications or the incorporation of functional nanomaterials to boost adsorption efficiency and durability. Additionally, embedding GP-NC in stable support matrices, such as polymer composites or encapsulated beads, could minimize material loss during regeneration and simplify handling in aqueous environments. Advanced fabrication techniques, like 3D printing, could also be explored to create structured adsorbents with optimized porosity and mechanical stability. Lastly, a life cycle assessment should be conducted to evaluate the environmental impact and long-term sustainability of GP-NC, ensuring its viability for large-scale wastewater treatment applications.

4. Conclusion

This study explores the effectiveness of porous alkali-activated material (GP-NC) synthesized through geopolymerization, with the addition of hydrogen peroxide as a pore-forming agent, for removing MB cationic dye. XRD and ^{29}Si and ^{27}Al MAS NMR analyses confirmed the successful formation of alkali activated. FTIR results provided interesting evidence of the activation of natural clay by the activation solution. Meanwhile, DTA/TGA and BET confirmed the porosity enhancement. The performed

Table 5 Adsorption capacity of MB cationic dye of materials based geopolymer revealed in literature

Materials	m_{AD} (g L^{-1}); t (min); [MB] (mg L^{-1})	q_{max} (mg g^{-1})	Advantages	Disadvantages/limitations	Ref.
Cu_2O-geopolymer	1; 250; 32	14.8	Effective catalytic properties - functions as a photocatalyst or catalyst support in various reactions.	Risk of contamination - certain oxides in adsorbents may lead to soil, water, and plant contamination.	53
Cu_2O/TiO_2 geopolymer	1; 150; 32	14.8	Cost-Effective and eco-Friendly - Low-cost materials that reduce overall process expenses and environmental impact.	Limited catalytic applications - some adsorbents have restricted use in catalytic processes.	54
Mesoporous seawater-based geopolymer	0.08; 90; -.	59.52	Highly efficient in filtration and adsorption - suitable for water and air purification.	Adsorbent efficiency limitations - the efficiency of adsorbents may restrict their practical applications.	55
Porous coal gangue microsphere/geopolymer	4; 60 min; 100	24.6	Highly efficient in filtration and adsorption - suitable for water and air purification.	Adsorbent efficiency limitations - the efficiency of adsorbents may restrict their practical applications.	56
Biomass fly ash geopolymer monoliths	(Cylindrical discs: d = 22 mm and thickness = 3 mm); 30; 50	15.4	No strict quality requirements for fly ash adsorbents - can be used directly as membranes, unlike powdered adsorbents.	Limited adsorption capacity - some adsorbents may not retain sufficient contaminants for long-term use.	3
Magnetite/geopolymer	0.004; 30; 50	76.34	Abundant and renewable - readily available in nature and recyclable for sustainable applications.	Regeneration and reusability challenges - long-term performance and cost-effectiveness may be affected by reusability issues.	57
Metakaolin based geopolymer	1; 120; 40	43.48	Recyclable and readily renewable - these adsorbents are sustainable and environmentally friendly.	Limited adsorption capacity - some adsorbents may not effectively retain contaminants for extended use.	58
Phosphoric acid based geopolymers	0.4; 90; 50	4.9	Abundant in nature - widely available, ensuring sustainable and cost-effective supply.	Regeneration and reusability challenges - long-term performance and cost-effectiveness may be affected by repeated use.	59
PY-GP4	2.4; 120; 100	64.10	Low-cost adsorbents for wastewater treatment - affordable and can be directly applied in treatment processes.	Regeneration and reusability could limit long-term performance and cost-effectiveness.	6
GP-NC	3; 60; 100	98.95	Economical and environmentally friendly – these materials offer a cost-effective solution with minimal environmental impact.	Regeneration and reusability challenges - maintaining effectiveness over multiple cycles can be a challenge.	This work

m_{AD}: Adsorbent dose (g L^{-1}); t: contact time; [MB]: concentration of methylene blue.

adsorption experiments demonstrated that GP-NC offers excellent performance in eliminating MB from the solution. The adsorption test findings revealed several important points. Firstly, there is a direct correlation between the dose of GP-NC and the efficiency of MB removal; with higher concentrations leading to increased removal percentages due to enhanced availability of adsorption sites. The optimal GP-NC dose is determined to be 3 g L^{-1}, achieving an impressive 99.45% removal efficiency. Secondly, the effect of contact time suggests equilibrium for MB adsorption is reached at approximately 60 minutes, implying both external and internal mass transfer mechanisms play roles in the adsorption process. Thirdly, pH significantly influences MB adsorption, with alkaline conditions enhancing adsorption capacities due to electrostatic forces. The pseudo second order kinetic model and the Langmuir isotherm model provided the best fit for the sorption process, with a maximum adsorption capacity of 98.95 mg g^{-1} at 25 °C. Furthermore, the calculated mean of free energy (E) from the Dubinin-Radushkevich model confirms that the adsorption of MB onto GP-NC follows a physisorption mechanism. Comparisons with other adsorbents from literature underscore GP-NC's superior performance in MB dye removal, attributed to its unique surface charge and pore structure. In summary, GP-NC demonstrates exceptional efficacy in wastewater treatment, positioning it as a highly promising adsorbent material for cationic dye removal.

Data availability

Data will be made available on request.

Conflicts of interest

The authors declare that they have no known competing financial interests or personal relationships that could have appeared to influence the work reported in this paper.

References

1 S. Ghattavi and A. Nezamzadeh-Ejhieh, A double-Z-scheme ZnO/AgI/WO3 photocatalyst with high visible light activity: Experimental design and mechanism pathway in the degradation of methylene blue, *J. Mol. Liq.*, 2021, **322**, 114563, DOI: 10.1016/j.molliq.2020.114563.

2 J. R. Martins, R. M. N. D. Hotza and J. A. L. L. Senff, Waste - Derived Geopolymers for Artificial Coral Development by 3D Printing, *J. Sustain. Metall.*, 2025, **11**, 114–125, DOI: 10.1007/s40831-025-01016-3.

3 R. M. Novais, G. Ascensão, D. M. Tobaldi, M. P. Seabra and J. A. Labrincha, Biomass fly ash geopolymer monoliths for effective methylene blue removal from wastewaters, *J. Cleaner Prod.*, 2018, **171**, 783–794, DOI: 10.1016/j.jclepro.2017.10.078.

4 A. Chaoui, S. Farsad, A. Ben Hamou, A. Amjlef, N. Nouj, M. Ezzahery and N. El Alem, Reshaping environmental sustainability: Poultry by-products digestate valorization for enhanced biochar performance in methylene blue removal, *J. Environ. Manage.*, 2024, **351**, 119870, DOI: 10.1016/j.jenvman.2023.119870.

5 L. Mllaoiy, S. Bikerchalen, B. Akhsassi, O. Ouzaguine, B. Bakiz, S. Villain, A. Taoufyq, F. Guinneton, J. C. Valmalette, J. R. Gavarri and A. Benlhachemi, Engineering BiOBr nanoplatelets with {001} facet exposure: Synthesis, characterization and visible-light photocatalytic properties, *Ceram. Int.*, 2025, DOI: 10.1016/j.ceramint.2025.01.323.

6 Y. Ettahiri, L. Bouna, J. V. Hanna, A. Benlhachemi, H. L. Pilsworth, A. Bouddouch and B. Bakiz, Pyrophyllite clay-derived porous geopolymers for removal of methylene blue from aqueous solutions, *Mater. Chem. Phys.*, 2023, **296**, 127281, DOI: 10.1016/j.matchemphys.2022.127281.

7 K. Fritah, M. Khachane, A. Bouddouch and B. Akhsassi, New insight for enhanced photocatalytic activity of $Bi_{4-x}La_xTi_3O_{12}$ ($0 \leq x \leq 1$) solid solution: A case study on degradation of Rhodamine B under UV light irradiation, *Opt. Mater.*, 2024, **150**, 115182, DOI: 10.1016/j.optmat.2024.115182.

8 B. Akhsassi, A. Bouddouch, Y. Naciri, B. Bakiz, A. Taoufyq, C. Favotto, S. Villain, F. Guinneton and A. Benlhachemi, Enhanced photocatalytic activity of $Zn_3(PO_4)_2$/ZnO composite semiconductor prepared by different methods, *Chem. Phys. Lett.*, 2021, **783**, 139046, DOI: 10.1016/j.cplett.2021.139046.

9 B. Akhsassi, Y. Ettahiri, B. Bakiz, A. Taoufyq, S. Villain, C. Favotto, F. Guinneton, J.-R. Gavarri and A. Benlhachemi, Novel Z-scheme Bi3O4Cl/Bi24O31Cl10 2D/3D heterojunction for enhanced photocatalytic activity under visible light, *Colloids Surf., A*, 2023, **673**, 131762, DOI: 10.1016/j.colsurfa.2023.131762.

10 B. Akhsassi, A. Bouddouch, Y. Naciri, Y. Ettahiri, B. Bakiz, A. Taoufyq and S. Villain, Visible light-driven type II p-Bi3O4Cl/n-BiPO4 heterojunction for effective photocatalytic photodegradation, *Ceram. Int. J.*, 2024, **50**, 32338–32352, DOI: 10.1016/j.ceramint.2024.06.041.

11 A. Ben Hamou, M. Enneiymy, S. Farsad, A. Amjlef, A. Chaoui, N. Nouj, A. Majdoub, A. Jada and M. Ez-Zahery, N. El Alem, Novel chemically reduced cobalt-doped g-C3N4 (CoCN-x) as a highly heterogeneous catalyst for the super-degradation of organic dyes *via* peroxymonosulfate activation, *Mater. Adv.*, 2024, **5**, 1960–1976, DOI: 10.1039/d3ma00818e.

12 N. Iberache, F. E. Titchou, M. Errami, S. Ben-Aazza, A. Driouiche, R. A. Akbour, M. Hamdani and A. Hadfi, Removal of the Insecticide Imidacloprid from Water in Commercial Formulation using Electro-Fenton and Photo-Electro-Fenton: Optimization of COD Removal through Response Surface Methodology RSM-CCD, *Chem. Eng. Process.*, 2024, **196**, 109633, DOI: 10.1016/j.cep.2023.109633.

13 Y. Ettahiri, B. Akhsassi, M. El, A. Bouddouch, L. Bouna, A. Benlhachemi, P. Luis, R. De F and M. Moreira, From synthesis to applications: A comprehensive review of geopolymer materials for photocatalytic degradation of organic pollutants, *Sep. Purif. Technol.*, 2024, **330**, 125396, DOI: 10.1016/j.seppur.2023.125396.

14 M. Farsi and A. Nezamzadeh-Ejhieh, A Z-scheme Cobalt(II) oxide-silver tungstate nano photocatalyst: Experimental

design and mechanism study for the degradation of methylene blue, *Surf. Interfaces*, 2022, **32**, 102148, DOI: 10.1016/j.surfin.2022.102148.

15 Y. Ettahiri, B. Bouargane, K. Fritah, B. Akhsassi, L. Pérez-Villarejo, A. Aziz, L. Bouna, A. Benlhachemi and R. M. Novais, A state-of-the-art review of recent advances in porous geopolymer: Applications in adsorption of inorganic and organic contaminants in water, *Constr. Build. Mater.*, 2023, **395**, 119870, DOI: 10.1016/j.conbuildmat.2023.132269.

16 Y. Ettahiri, L. Bouna, A. Brahim, A. Benlhachemi, B. Bakiz, D. Eliche-quesada, P. Luis, B. Bakiz and J. S. Pedro, Synthesis and characterization of porous and photocatalytic geopolymers based on natural clay: Enhanced properties and efficient Rhodamine B decomposition, *Appl. Mater. Today*, 2024, **36**, 102048, DOI: 10.1016/j.apmt.2023.102048.

17 Y. Wang, L. Liu, C. Ren, J. Ma, B. Shen, P. Zhao and Z. Zhang, A novel amine functionalized porous geopolymer spheres from municipal solid waste incineration fly ash for CO_2 capture, *J. Environ. Manage.*, 2024, **349**, 119540, DOI: 10.1016/j.jenvman.2023.119540.

18 G. A. Tochetto, L. Simão, D. de Oliveira, D. Hotza and A. P. S. Immich, Porous geopolymers as dye adsorbents: Review and perspectives, *J. Cleaner Prod.*, 2022, **374**, 133982, DOI: 10.1016/j.jclepro.2022.133982.

19 L. Bouna, Y. Ettahiri, A. Elimbi, A. Benlhachemi and M. Cyr, Role of washing process in the improvement of surface properties of porous geopolymers, *J. Porous Mater.*, 2022, **31**, 569–576, DOI: 10.1007/s10934-023-01533-0.

20 R. M. Novais, R. C. Pullar and J. A. Labrincha, Geopolymer foams: An overview of recent advancements, *Prog. Mater. Sci.*, 2020, **109**, 100621, DOI: 10.1016/j.pmatsci.2019.100621.

21 P. Delgado-Plana, A. García-Díaz, S. Bueno-Rodríguez and D. Eliche Quesada, Influence of NaOH molarity and Portland cement addition on performance of alkali activated cements based in silicomanganese slags, *Constr. Build. Mater.*, 2023, **407**, 133544, DOI: 10.1016/j.conbuildmat.2023.133544.

22 B. A. Tayeh, A. Hakamy, M. Amin, A. M. Zeyad and I. S. Agwa, Effect of air agent on mechanical properties and microstructure of lightweight geopolymer concrete under high temperature, *Case Stud. Constr. Mater.*, 2022, **16**, e00951, DOI: 10.1016/j.cscm.2022.E00951.

23 M. Ben ali, H. El Fadili, M. El Mahi, A. Aziz, A. Moussadik, S. Devkota and E. M. Lotfi, Preparation of greener geopolymer binder based fly ash: An effective strategy toward carbon neutrality, *Ceram. Int.*, 2024, **50**, 27018–27026, DOI: 10.1016/j.ceramint.2024.04.434.

24 A. García-Díaz, S. Bueno-Rodríguez, L. Pérez-Villarejo and D. Eliche-Quesada, Reuse of Oil Refining Sludge Residue Ash *via* Alkaline Activation in Matrices of Chamotte or Rice Husk Ash, *Materials*, 2023, **16**, 2801, DOI: 10.3390/ma16072801.

25 R. M. Novais, J. Carvalheiras, D. M. Tobaldi, M. P. Seabra, R. C. Pullar and J. A. Labrincha, Synthesis of porous biomass fly ash-based geopolymer spheres for efficient removal of methylene blue from wastewaters, *J. Cleaner Prod.*, 2019, **207**, 350–362, DOI: 10.1016/j.jclepro.2018.09.265.

26 L. Bouna, A. Ait El Fakir, A. Benlhachemi, K. Draoui, M. Ezahri, B. Bakiz, S. Villain, F. Guinneton and N. Elalem, Synthesis and characterization of mesoporous geopolymer based on Moroccan kaolinite rich clay, *Appl. Clay Sci.*, 2020, **196**, 105764, DOI: 10.1016/j.clay.2020.105764.

27 X. Ma, D. Xu, Y. Li, Z. Ou and A. Howard, Synthesis of a new porous geopolymer from foundry dust to remove Pb2+ and Ni^{2+} from aqueous solutions, *J. Cleaner Prod.*, 2022, **349**, 131488, DOI: 10.1016/j.jclepro.2022.131488.

28 Y. Fang, L. Yang, F. Rao, Y. Zheng and Z. Song, Adsorption behavior and mechanism of MB, Pb(II) and Cu(II) on porous geopolymers, *Ceram. Int.*, 2025, 1–12, DOI: 10.1016/j.ceramint.2024.12.564.

29 S. Petlitckaia and A. Poulesquen, Design of lightweight metakaolin based geopolymer foamed with hydrogen peroxide, *Ceram. Int.*, 2019, **45**, 1322–1330, DOI: 10.1016/j.ceramint.2018.10.021.

30 S. Berred, D. Fadli, F. Di Gregorio and K. Berred, Geological and landscape particularities of Issafen-style chevron pattern in Tata region (Anti-Atlas, South Morocco), *Arab. J. Geosci.*, 2020, **13**, 689, DOI: 10.1007/s12517-020-05713-z.

31 N. Fiol and I. Villaescusa, Determination of sorbent point zero charge: Usefulness in sorption studies, *Environ. Chem. Lett.*, 2009, **7**, 79–84, DOI: 10.1007/s10311-008-0139-0.

32 Y. Ettahiri, D. M. Samuel, L. Bouna, A. Khali, A. Aziz, A. Benlhachemi, L. Pérez-Villarejo and W. M. Kriven, Comparative study of physicochemical properties of geopolymers prepared by four Moroccan natural clays, *J. Build. Eng.*, 2023, **80**, 108021, DOI: 10.1016/j.jobe.2023.108021.

33 J. Davidovits, *Geopolymer CHemistry and Applications*, 5th edition, 2008. https://www.researchgate.net/publication/265076752.

34 J. Rocha and J. Klinowski, Solid-State NMR Studies of the Structure and Reactivity of Metakaolinite, *Angew. Chem., Int. Ed. Engl.*, 1990, **29**, 553–554, DOI: 10.1002/anie.199005531.

35 D. Massiot, P. Dion, J. F. Alcover and F. Bergaya, 27Al and 29Si MAS NMR Study of Kaolinite Thermal Decomposition by Controlled Rate Thermal Analysis, *J. Am. Ceram. Soc.*, 1995, **78**, 2940–2944, DOI: 10.1111/j.1151-2916.1995.tb09067.x.

36 Y. L. Tsai, J. V. Hanna, Y. L. Lee, M. E. Smith and J. C. C. Chan, Solid-state NMR study of geopolymer prepared by sol-gel chemistry, *J. Solid State Chem.*, 2010, **183**, 3017–3022, DOI: 10.1016/j.jssc.2010.10.008.

37 A. Á. B. Maia, R. S. Angélica, R. de Freitas Neves, H. Pöllmann, C. Straub and K. Saalwächter, Use of 29Si and 27Al MAS NMR to study thermal activation of kaolinites from Brazilian Amazon kaolin wastes, *Appl. Clay Sci.*, 2014, **87**, 189–196, DOI: 10.1016/j.clay.2013.10.028.

38 J. G. S. V. A. N. Jaarsveld, J. S. J. V. A. N. Deventer and G. C. Lukey, A Comparative Study Of Kaolinite Versus Metakaolinite In Fly Containing Immobilized, *Chem. Eng.*

Commun., 2010, **191**, 531–549, DOI: **10.1080/00986440490277974**.

39 S. Prasanphan, K. Hemra and A. Wannagon, 29 Si and 27 Al NMR study of the structural transformation of calcined kaolin residue-based geopolymer using low alkali activator content for sustainable construction materials, *J. Build. Eng.*, 2023, **70**, 106332, DOI: **10.1016/j.jobe.2023.106332**.

40 T. R. Barbosa, E. L. Foletto, G. L. Dotto and S. L. Jahn, Preparation of mesoporous geopolymer using metakaolin and rice husk ash as synthesis precursors and its use as potential adsorbent to remove organic dye from aqueous solutions, *Ceram. Int.*, 2018, **44**, 416–423, DOI: **10.1016/j.ceramint.2017.09.193**.

41 M. al S. Shafiof and A. Nezamzadeh-Ejhieh, A comprehensive study on the removal of Cd(II) from aqueous solution on a novel pentetic acid-clinoptilolite nanoparticles adsorbent: Experimental design, kinetic and thermodynamic aspects, *Solid State Sci.*, 2020, **99**, 106071, DOI: **10.1016/j.solidstatesciences.2019.106071**.

42 H. T. Dzoujo, V. O. Shikuku, S. Tome, S. Akiri, N. M. Kengne, S. Abdpour, C. Janiak, M. A. Etoh and D. Dina, Synthesis of pozzolan and sugarcane bagasse derived geopolymer-biochar composites for methylene blue sequestration from aqueous medium, *J. Environ. Manage.*, 2022, **318**, 115533, DOI: **10.1016/j.jenvman.2022.115533**.

43 L. Bouna, A. A. El Fakir, Y. Ettahiri, H. Abara, A. Jada, K. Draoui, A. Benlhachemi and M. Ezahri, Understanding the impact of kaolinite/muscovite ratio in natural clays on oxide contents, physisorbed water, and structural water fractions, *Mater. Chem. Phys.*, 2024, **314**, 128858, DOI: **10.1016/j.matchemphys.2023.128858**.

44 S. Selmani, A. Sdiri, S. Bouaziz, E. Joussein and S. Rossignol, Effects of metakaolin addition on geopolymer prepared from natural kaolinitic clay, *Appl. Clay Sci.*, 2017, **146**, 457–467, DOI: **10.1016/j.clay.2017.06.019**.

45 Z. Ji, L. Su and Y. Pei, Characterization and adsorption performance of waste-based porous open-cell geopolymer with one-pot preparation, *Ceram. Int.*, 2021, **47**, 12153–12162, DOI: **10.1016/j.ceramint.2021.01.062**.

46 A. Autef, E. Joussein, G. Gasgnier, S. Pronier, I. Sobrados, J. Sanz and S. Rossignol, Role of metakaolin dehydroxylation in geopolymer synthesis, *Powder Technol.*, 2013, **250**, 33–39, DOI: **10.1016/j.powtec.2013.09.022**.

47 W. Li, L. Wang, C. Bai, Y. Ren and P. Colombo, In situ growth of CuO on porous geopolymer spheres as green catalysts for enhanced peroxymonosulfate-activated degradation of Orange I, *J. Am. Ceram. Soc.*, 2024, **107**, 2143–2154, DOI: **10.1111/jace.19616**.

48 S. Yan, X. Ren, F. Zhang, K. Huang, X. Feng and P. Xing, Comparative study of Pb^{2+}, Ni^{2+}, and methylene blue adsorption on spherical waste solid-based geopolymer adsorbents enhanced with carbon nanotubes, *Sep. Purif. Technol.*, 2022, **284**, 120234, DOI: **10.1016/j.seppur.2021.120234**.

49 P. Ghahremani, M. H. Vakili and A. Nezamzadeh-Ejhieh, Optimization of Pb(II) removal by a novel modified silica aerogel using Quince seed mucilage with response surface methodology, *J. Environ. Chem. Eng.*, 2021, **9**, 106648, DOI: **10.1016/j.jece.2021.106648**.

50 P. Ghahremani, A. Nezamzadeh-Ejhieh and M. H. Vakili, A comparison of adsorption capacity of several synthesis methods of cellulose-based absorbent towards Pb(II) removal: Optimization with response surface methodology, *Int. J. Biol. Macromol.*, 2023, **253**, 127115, DOI: **10.1016/j.ijbiomac.2023.127115**.

51 V. S. Munagapati, J. C. Wen, C. L. Pan, Y. Gutha, J. H. Wen and G. M. Reddy, Adsorptive removal of anionic dye (Reactive Black 5) from aqueous solution using chemically modified banana peel powder: kinetic, isotherm, thermodynamic, and reusability studies, *Int. J. Phytoremediation.*, 2020, **22**, 267–278, DOI: **10.1080/15226514.2019.1658709**.

52 M. Anari-Anaraki and A. Nezamzadeh-Ejhieh, Modification of an Iranian clinoptilolite nano-particles by hexadecyltrimethyl ammonium cationic surfactant and dithizone for removal of Pb(II) from aqueous solution, *J. Colloid Interface Sci.*, 2015, **440**, 272–281, DOI: **10.1016/j.jcis.2014.11.017**.

53 M. Fallah, K. J. D. MacKenzie, J. V. Hanna and S. J. Page, Novel photoactive inorganic polymer composites of inorganic polymers with copper(I) oxide nanoparticles, *J. Mater. Sci.*, 2015, **50**, 7374–7383, DOI: **10.1007/S10853-015-9295-3**.

54 M. Falah and K. J. D. MacKenzie, Synthesis and properties of novel photoactive composites of P25 titanium dioxide and copper (I) oxide with inorganic polymers, *Ceram. Int.*, 2015, **41**, 13702–13708, DOI: **10.1016/j.ceramint.2015.07.198**.

55 M. Padmapriya, S. T. Ramesh and V. M. Biju, Synthesis of seawater based geopolymer: Characterization and adsorption capacity of methylene blue from wastewater, *Mater. Today Proc.*, 2022, **51**, 1770–1776, DOI: **10.1016/j.matpr.2021.03.030**.

56 S. Yan, P. He, D. Jia, Q. Wang, J. Liu, J. Yang and Y. Huang, Synthesis of novel low-cost porous gangue microsphere/geopolymer composites and their adsorption properties for dyes, *Int. J. Appl. Ceram. Technol.*, 2018, **15**, 1602–1614, DOI: **10.1111/ijac.13045**.

57 R. A. Al-husseiny and S. E. Ebrahim, Effective Removal of Methylene Blue from Wastewater Using Magnetite/Geopolymer Composite: Synthesis, Characterization and Column Adsorption Study, *Inorg. Chem. Commun.*, 2022, **139**, 109318, DOI: **10.1016/j.inoche.2022.109318**.

58 M. El Alouani, S. Alehyen, M. El Achouri and M. Taibi, Preparation, Characterization, and Application of Metakaolin-Based Geopolymer for Removal of Methylene Blue from Aqueous Solution, *J. Chem.*, 2019, **2019**, 14, DOI: **10.1155/2019/4212901**.

59 M. I. Khan, T. K. Min, K. Azizli, S. Sufian, H. Ullah and Z. Man, Effective removal of methylene blue from water using phosphoric acid based geopolymers: Synthesis, characterizations and adsorption studies, *RSC Adv.*, 2015, **5**, 61410–61420, DOI: **10.1039/c5ra08255b**.